Energy Advances

ROYAL SOCIETY OF CHEMISTRY

PAPER

View Article Online
View Journal | View Issue

Check for updates

Cite this: *Energy Adv.*, 2024, 3, 874

Identifying the charge storage mechanism in polyimide anodes for Na-ion aqueous batteries by impedance spectroscopy†

Raphael L. Streng,[a] Sergei Vagin,[bc] Yuejie Guo,[a] Bernhard Rieger [c] and Aliaksandr S. Bandarenka *[ab]

Received 19th January 2024,
Accepted 20th March 2024

DOI: 10.1039/d4ya00037d

rsc.li/energy-advances

Polyimides such as poly(naphthalene four formyl ethylenediamine) (PNFE) demonstrate promising electrochemical properties as anode materials for aqueous sodium-ion batteries. They display high specific capacities and good cyclability. Still, an accurate physical model describing the exact charge storage mechanism in these electroactive polymers needs to be explored in more detail. This work aims to address this gap through an impedance study to elucidate the mechanisms of reduction and oxidation processes of polyimide electrodes. An electrochemical impedance model is also proposed, which enables good fitting of the impedance data at all potentials. This model confirms the commonly accepted two-stage enolization reaction as the main reduction path and also unveils a previously unrecognized single-electron pathway. A complete model was identified by including this novel pathway, which enabled a better understanding of these materials.

Open Access Article. Published on 21 March 2024. Downloaded on 5/25/2025 12:31:04 AM.
This article is licensed under a Creative Commons Attribution 3.0 Unported Licence.

1. Introduction

In times of rising demand for sustainable energy storage solutions, rechargeable batteries have become crucial in transitioning towards a renewable energy economy and powering modern technologies.[1,2] Among various systems, lithium-ion batteries (LIBs) are currently dominating the market, as they offer high energy and power densities, which are essential for application in electric vehicles and mobile devices.[3,4] However, the limited supply of lithium as well as the inherent safety issues of LIBs, have motivated a recent interest in alternative battery technologies.[5–8] Recent advances in battery research include Li-free systems utilizing more abundant alkali metals such as Na,[9–11] as well as safer aqueous electrolytes.[12,13] Combining their advantages, aqueous sodium-ion batteries (ASIBs) have attracted increased attention due to their potential to complement and even replace LIBs, especially in stationary energy storage applications. The natural abundance of sodium and the intrinsic safety, high ionic conductivity, and low cost of the aqueous electrolyte can make them favorable for these systems.[14–18] However, the larger size of sodium ions and the electrochemical stability window of water limit the choice of electrode materials. Various compounds, such as Prussian blue analogs,[19,20] manganese oxides,[21–23] and polyanionic compounds[10,11,13] offer superior stability and fast charging performance as cathodes for ASIBs. However, only a few suitable anode materials for ASIBs have been reported besides the transition metal-based NASICON-type $NaTi_2(PO_4)_3$[24,25] and the Prussian blue analog manganese hexacyanomanganate.[23]

Redox-active organic materials can be a sustainable, inexpensive, and high-performance alternative to inorganic compounds that often contain scarce or polluting elements.[26,27] Polyimides (PIs) have emerged as a promising anode material for aqueous metal-ion batteries due to their low electrode potential, high cycling stability, and superior specific capacity.[28,29] In addition, they exhibit remarkable mechanical strength, thermal resistance, and chemical stability and are fully compatible with aqueous electrolytes.[24]

Whereas the exceptional electrochemical performance of PIs has been reported several times,[28–30] a more detailed examination of the underlying charge transfer processes should be further performed. Ultimately, understanding the charge storage mechanism in PIs is of great importance to unlock their full potential and accelerate their application in practical systems. Electrochemical impedance spectroscopy (EIS) is a non-destructive, non-invasive, and fast technique that can reveal charge transfer mechanisms and characterize degradation as well as mass transport processes.[31] By applying a low amplitude sinusoidal voltage or current signal over a certain

[a] *Physics of Energy Conversion and Storage, Department of Physics, Technische Universität München, James-Franck-Str. 1, 85748 Garching, Germany. E-mail: bandarenka@ph.tum.de*
[b] *Catalysis Research Center TUM, Ernst-Otto-Fischer-Straße 1, 85748 Garching, Germany*
[c] *WACKER-Lehrstuhl für Makromolekulare Chemie, Department of Chemistry, Technische Universität München, Lichtenbergstraße 4, 85748 Garching, Germany*

† Electronic supplementary information (ESI) available. See DOI: https://doi.org/10.1039/d4ya00037d

© 2024 The Author(s). Published by the Royal Society of Chemistry

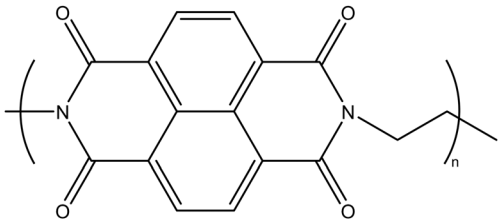

Fig. 1 Chemical structure of poly(naphthalene four formyl ethylenediamine) (PNFE).

Open Access Article. Published on 21 March 2024. Downloaded on 5/25/2025 12:31:04 AM. This article is licensed under a Creative Commons Attribution 3.0 Unported Licence.

frequency range, EIS can fully extract any information on the impedances in the cell. However, to understand the data, it is essential to interpret the spectrum with an accurate physical model, often expressed for simplicity in terms of equivalent electric circuits (EECs).[32] Thus, for each electrode, complete EECs that describe the physical processes in a meaningful way need to be created. These models can then be combined to gain information on the full battery.

This work provides new insight into the redox mechanism of the electrode material poly(naphthalene four formyl ethylenediamine) (PNFE, see Fig. 1) by subjecting it to an in-depth EIS study.

2. Experimental

2.1. Synthesis of PNFE

All utilized chemicals were purchased from commercial suppliers and utilized without additional purification unless mentioned.

Poly(naphthalene four formyl ethylenediamine) was prepared according to literature procedure with minor modification.[28] In brief, 1,4,5,8-naphthalene tetracarboxylic dianhydride (NTCDA, 2.68 g, 10 mmol) and ethylenediamine (EDA, 0.6 g, 10 mmol) were mixed with 20 ml of degassed *N*-methyl pyrrolidone (NMP) in a Schlenk flask. The flask was equipped with an air-cooled condenser and an overpressure valve on top, and the reaction mixture was heated overnight in a sand bath at a bath temperature set to 215 °C. After cooling, the dark precipitate was filtered off and washed thoroughly with NMP and subsequently with water. It was dried *in vacuo* with a stepwise increase of drying temperature (room temperature, 120 °C and 210 °C) to a constant vacuum of 0.08 mbar yielding 2.7 g (92%) of grey-brownish powder.

Elemental analysis: calcd for an infinite polyimide ($C_{16}H_8N_2O_4$), %: C 65.76, H 2.76, N 9.59; calcd for an octamer, %: C 65.10, H 3.03, N 10.52; found, %: C 65.13, H 2.91, N 10.32.

2.2. Structural characterization

The chemical structure of the obtained polymer was characterized *via* Fourier-transformed infrared (FTIR) spectroscopy using a Bruker Vertex-70 spectrometer equipped with a Platinum-ATR-accessory. To analyze the morphology of the film a field emission scanning electron microscope (SEM, JSM-7500F, JEOL) was employed. Thermogravimetric analysis (TGA) was carried out in argon using a METTLER TOLEDO TGA/DSC 2 (STARe system). A temperature range from 30 °C to 800 °C and a heating rate of 10 °C min^{-1} was chosen. X-ray photoelectron spectroscopy (XPS) spectra of the PNFE electrode were conducted using a non-monochromatized Al Kα source (1486.7 eV) on a SPECS setup (SPECS XR50 Xf-Ray source, SPECS PHOIBOS 150 hemispherical analyzer, SPECS spectrometer). The XPS spectra were fitted in the Casa XPS software (Version 2.3.24PR1.0). The binding energies were corrected by referencing the C–C peak of the C 1s spectrum to 284.8 eV.

2.3. Electrode preparation

The electrodes were prepared by the slurry casting method as follows. 80 wt% of the polyimide active material was ground with 10 wt% carbon black (MTI, USA) and 10 wt% Nafion™ binder (5 wt% in lower aliphatic alcohols and water, Sigma Aldrich, USA) in a planetary ball mill. Isopropyl alcohol and water in a 1 : 1 ratio were added under vigorous stirring to form the slurry, which was subsequently coated onto a pyrolytic graphite current collector with an active material mass loading of approximately 2.5 mg cm^{-2}. The so-prepared electrodes were dried overnight at room temperature before electrochemical measurements were performed. After drying, the electrode film thickness was determined to be 42 ± 3 μm.

2.4. Electrochemical measurements

Electrochemical measurements were conducted using a three-electrode glass cell with a constant argon flow to maintain an inert atmosphere. 8 M $NaClO_4$ was used as the electrolyte, as highly concentrated electrolytes are known to enhance electrode stability by preventing active material dissolution.[33,34] Before being run into the cell the electrolyte was purged with argon for approximately 10 minutes. The reference electrode utilized was an Ag/AgCl electrode (SSC, 3 M KCl, SI Analytics, "B 3420+"), connected to the electrolyte *via* a Luggin capillary. A platinum wire (MaTeck, Germany) was employed as the counter electrode.

CV (cyclic voltammetry) and EIS (electrochemical impedance spectroscopy) measurements were conducted using a BioLogic VSP-300 Potentiostat. To prevent any disturbances caused by the impedance of the reference electrode, a small shunt capacitor was connected between the reference electrode and an additional platinum wire, which was wrapped around the Luggin capillary and ended near it.

The cyclic voltammograms (CVs) were recorded at different scan rates ranging from 1 mV s^{-1} to 50 mV s^{-1} between 0 V *vs.* SSC and −1.1 V *vs.* SSC. Staircase electrochemical impedance spectroscopy was carried out in the same potential range in steps of 100 mV. Before recording the spectrum at each step, the potential was held for 10 minutes to ensure equilibrium conditions, which are vital for impedance measurements. A 10 mV AC amplitude was applied to the electrode with frequencies ranging from 1.00 MHz to 250 mHz. After the validity of the data was verified by Kramers–Kronig analysis, the spectra were fitted using the EIS Data Analysis 2.1 software.[35]

Open Access Article. Published on 21 March 2024. Downloaded on 5/25/2025 12:31:04 AM.
This article is licensed under a Creative Commons Attribution 3.0 Unported Licence.

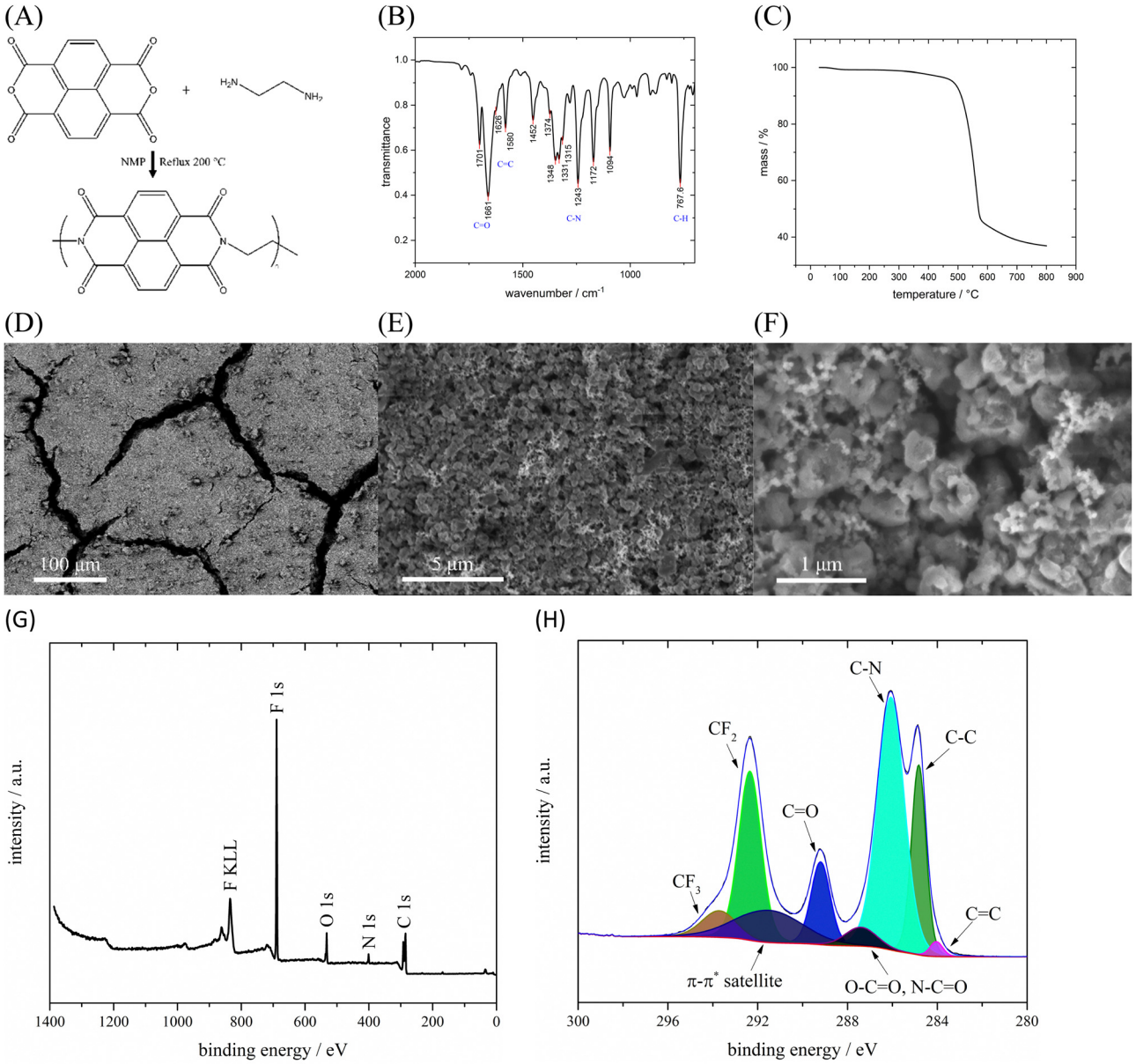

Fig. 2 (A) Synthesis route, (B) FTIR spectrum, and (C) TGA curve of PNFE. (D)–(F) SEM pictures of the PNFE slurry coated on a pyrolytic graphite sheet at different magnifications. (G) XPS survey spectrum of the PNFE slurry electrode. (H) Fitted XPS spectrum of the C 1s region of the PNFE slurry electrode.

3. Results and discussion

PNFE was synthesized using a simple one-step dehydration condensation reaction between NTCDA and EDA in NMP as shown in Fig. 2(A). The chemical structure of the as-prepared polymer was confirmed by FTIR-spectroscopy. The FTIR spectrum of the PNFE polymer is depicted in Fig. 2(B). The observed peaks are in good accordance with the expected structure of the synthesized polymer. Notably, the bands at 1701 cm^{-1} and 1661 cm^{-1} correspond to stretching vibrations of the C=O bonds in the electrochemically active carbonyl groups. Furthermore, characteristic stretching vibrations of the C=C bonds in the cyclic alkenes (1626 cm^{-1} and 1580 cm^{-1}) and various vibrations of aromatic and non-aromatic C–N bonds (1348 cm^{-1} to 1094 cm^{-1}) can be observed. The remaining spectral bands can be attributed to vibrations of C–H bonds in the polymer.

Fig. 2(C) shows the TGA curve of PNFE. The small initial mass loss is caused by the evaporation of residual water within the active material. Decomposition of the polymer can only be observed at a temperature of approximately 500 °C which confirms the excellent thermal stability of PNFE. To analyze the morphology of the PNFE electrode scanning electron microscopy (SEM) was conducted. It reveals a relatively even distribution of polymer agglomerates, which are typically less than 1 μm in size, as shown in Fig. 2(D–F). Together with the Nafion™ binder and the carbon black, the active material forms a porous film with pore sizes in the nm to μm range. To further analyze the surface structure of the PNFE electrodes, XPS

© 2024 The Author(s). Published by the Royal Society of Chemistry

Open Access Article. Published on 21 March 2024. Downloaded on 5/25/2025 12:31:04 AM.
This article is licensed under a Creative Commons Attribution 3.0 Unported Licence.

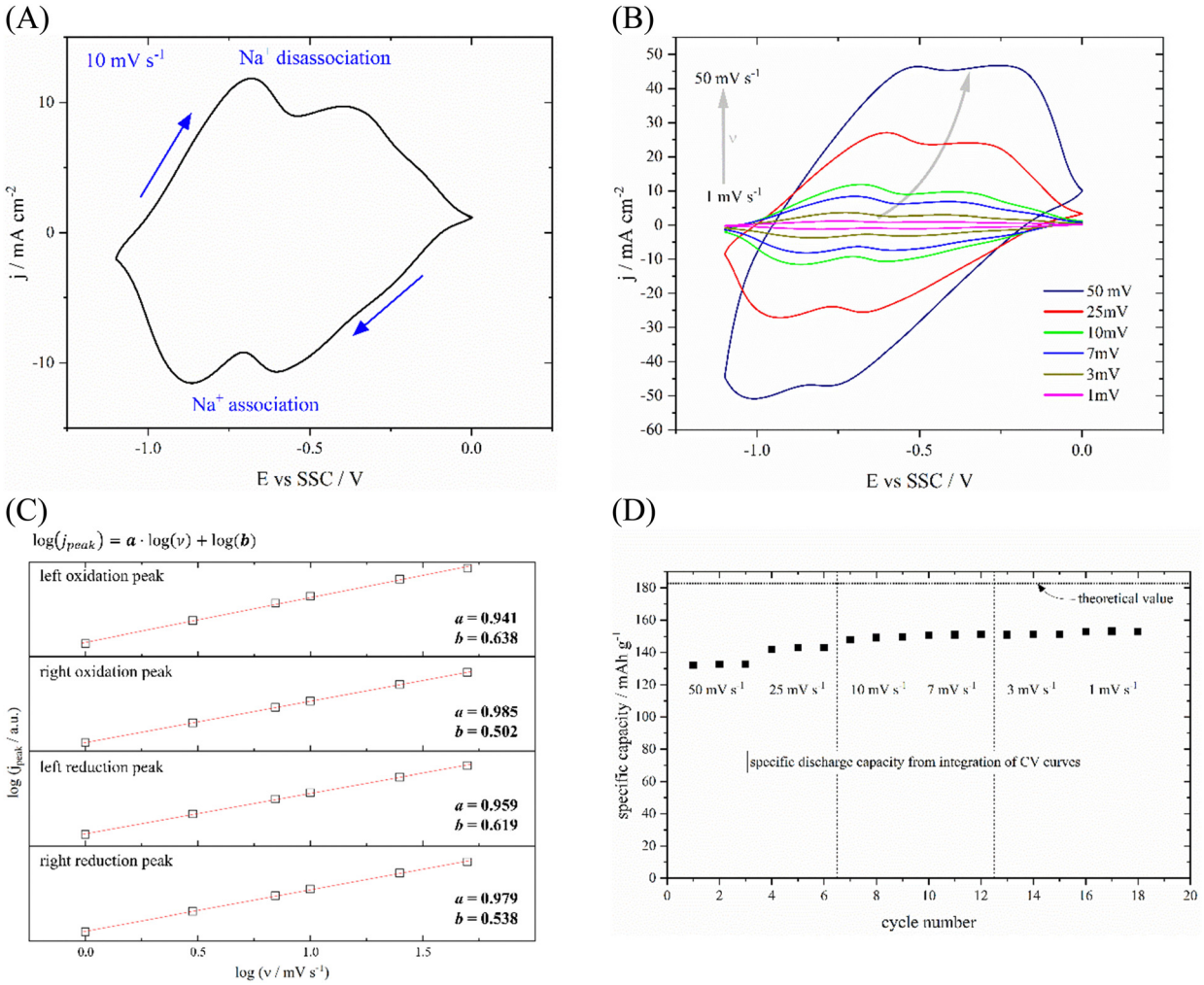

Fig. 3 (A) Cyclic voltammogram of the PNFE film coated on a pyrolytic graphite sheet in 8 M $NaClO_4$ recorded at 10 mV s^{-1}. (B) CVs recorded at different scan rates. (C) Dependence of the peak current on the scan rate for all four peaks. (D) Specific discharge capacity calculated by integrating the CV curves at different scan rates.

spectra were recorded. The survey scan depicted in Fig. 2(G) shows characteristic peaks for carbon, nitrogen, oxygen, and fluorine. Carbon and oxygen are part of the active material and the binder, whereas nitrogen and fluorine can be attributed to PNFE and Nafion™, respectively. In the C 1s spectrum (Fig. 2(H)), multiple peaks can be observed. The sharp peaks at 284.8 eV, 286.1 eV, 289.2 eV, and 292.4 eV correspond to C–C, C–N, C═O, and CF_2 bonds, respectively. The weaker peaks at 284.3, 287.4, and 293.8 are attributed to C═C, O–C═O or N–C═O, and CF_3. In addition, the extended delocalized electrons in the aromatic rings of PNFE result in a π–π* satellite structure at 291.5 eV. These results indicate that the active material and the binder are both present at the surface of the electrode, which is necessary to ensure mechanical stability as well as electrolyte access.

The electrochemical properties as well as the rate dependence of PNFE were investigated by measuring CVs at various scan rates. A typical CV recorded at 10 mV s^{-1} is shown in Fig. 3(A). Two separate pairs of reduction and oxidation peaks can be clearly distinguished. The oxidation peaks lie at −0.68 V

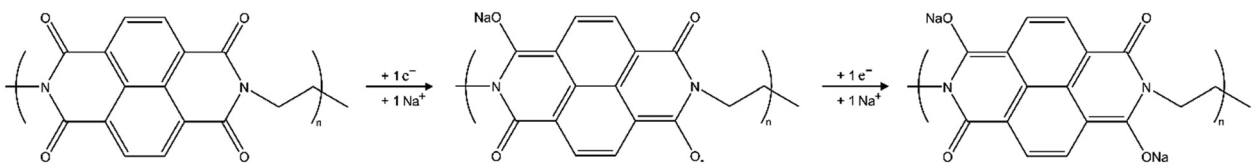

Fig. 4 Reduction mechanism of PNFE. In the first step, a radical anion is formed, followed by the generation of the dianion in the second step. Further reduction (3 or 4 electrons) is possible but only occurs at much lower potentials.[38]

Open Access Article. Published on 21 March 2024. Downloaded on 5/25/2025 12:31:04 AM.
This article is licensed under a Creative Commons Attribution 3.0 Unported Licence.

vs. SSC and −0.39 V *vs.* SSC respectively. The reduction peaks are close at −0.87 V *vs.* SSC and −0.61 V *vs.* SSC implying a reversible redox reaction. This double-peak structure supports the two-electron reduction mechanism which is commonly reported for PNFE and similar polyimides.[36,37] As shown in Fig. 4, the reduction leads to a two-step enolization reaction of two opposite carbonyl groups. In the first step, a radical anion is formed followed by the formation of the di-anion which allows it to adsorb two sodium ions. It should be noted that this is the generally accepted scheme for ion adsorption at carbonyl-based organic electrode materials. Since there are four carbonyl groups, one may expect further reduction by up to four electrons. Whereas this is generally possible, it only occurs at much lower potentials and thus below the hydrogen evolution reaction (HER) threshold.[38] The relatively wide expansion of the peaks in the *x*-direction suggests repulsive interactions between the two redox centers preventing the resolution of the two separate electron transfers. Therefore, a full understanding of the redox mechanism is only accessible by employing additional techniques. Here we use EIS to reveal the underlying processes.

Fig. 3(B) shows the CVs of PNFE at different scan rates between 1 and 50 mV s^{-1}. The peak-to-peak separation ΔE_{p-p} increases with increasing scan rate, which is mostly linked to the uncompensated resistance stemming from the electrolyte's ionic conductivity. However, it becomes clear that the charge transfer mechanism is highly reversible as ΔE_{p-p} drops to 59 mV at a scan rate of 1 mV s^{-1} for both pairs of peaks. By relating the peak current i_{peak} to the scan rate ν it is possible to deduce information on the processes limiting the charge transfer and, therefore, determine the current response in the CVs:

$$i_{peak} = b \cdot \nu^{a} \Rightarrow \log(i_{peak}) = \log(b) + a \cdot \log(\nu) \quad (1)$$

Hereby, the value of the parameter a ranges from 0.5 for fully mass transport limited processes to 1.0 for fully surface limited processes. As shown in Fig. 3(C) a lies close to 1.0 for all peaks within the investigated scan rate range implying low mass transport limitations. Due to the high concentration of the 8 M $NaClO_4$ electrolyte, the faradaic current is not impaired by the diffusion of ions toward the electrode surface. However, at higher scan rates, a slightly lower value for a can be observed, as can be expected for slurry electrodes with higher mass loadings. This is most likely caused by the diffusion of Na^+ within the film, which will be discussed in more detail in the EIS analysis.

The total transferred charge within one cycle can be calculated by integrating the CVs. Fig. 3(D) shows that a maximum specific discharge capacity of *ca.* 153 mA h g^{-1} is measured at the slowest scan rates. As indicated by the dotted line, this value is significantly lower than the theoretical specific capacity of PNFE for a two-electron charge transfer. This observation is in accordance with previous studies on various polyimides, which consistently report capacities considerably below the

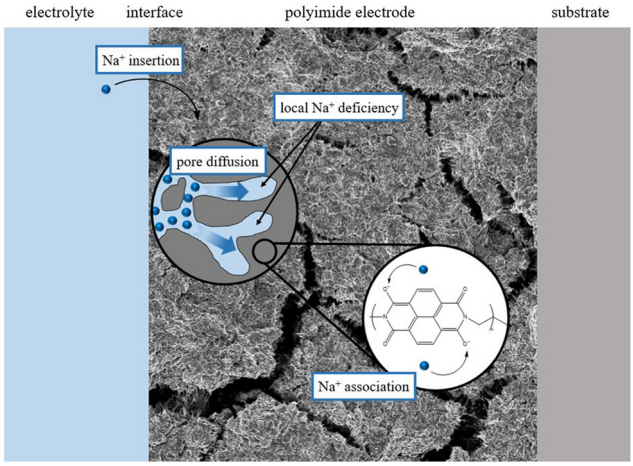

Fig. 6 Diffusion limitations arise due to local Na^+ deficiency in the pores of the slurry. Even with the highly concentrated electrolyte, the diffusion through the small pores is too slow to compensate for concentration gradients immediately.

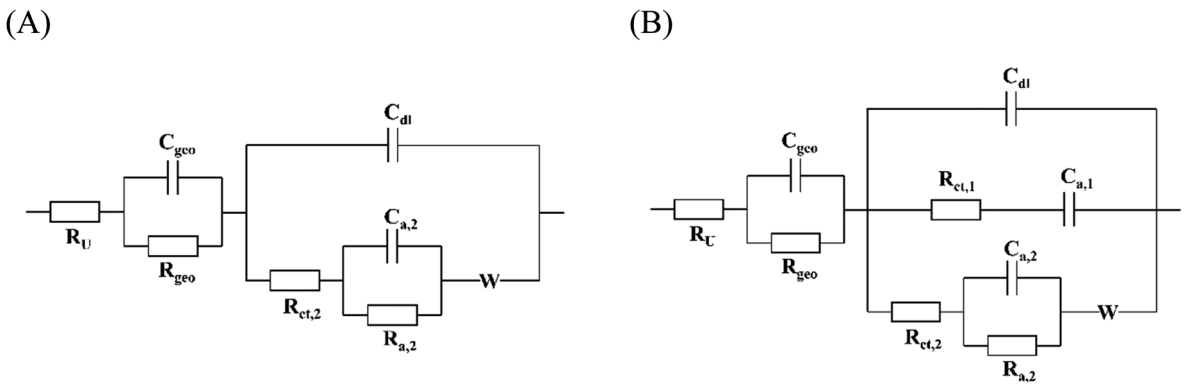

Fig. 5 (A) EEC describing a two-stage conjugated mechanism with reversible stages. It includes the electrolyte resistance (R_U), the impedances of the capacitance of the film (R_{geo}, C_{geo}), of the double layer (C_{dl}), and the two-stage mechanism ($R_{ct,2}$, $C_{a,2}$, $R_{a,2}$) as well as a Warburg element modeling diffusion of Na^+ ions inside the pores of the slurry (W). (B) The EEC used to fit the data additionally includes the impedance of the parallel single-stage mechanism ($R_{ct,1}$, $C_{a,1}$).

© 2024 The Author(s). Published by the Royal Society of Chemistry

Open Access Article. Published on 21 March 2024. Downloaded on 5/25/2025 12:31:04 AM.
This article is licensed under a Creative Commons Attribution 3.0 Unported Licence.

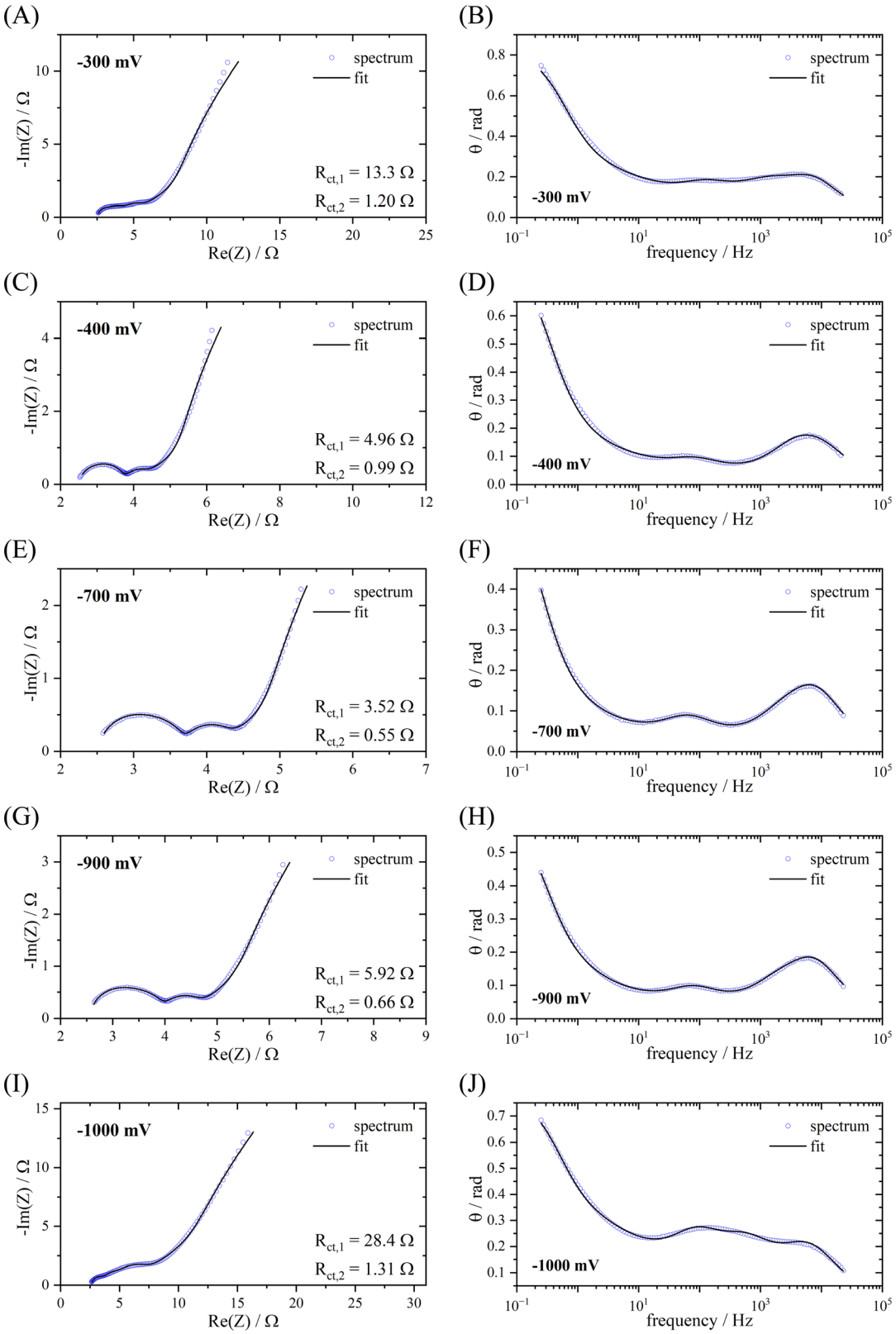

Fig. 7 Fitted EIS spectra of PNFE at different potentials *vs.* SSC. The graphs on the left show the Nyquist plots (A), (C), (E), (G) and (I). The graphs on the right show the dependence of the phase shift Θ on the frequency (B), (D), (F), (H) and (J). For fitting the EEC in Fig. 5(B) was used.

Open Access Article. Published on 21 March 2024. Downloaded on 5/25/2025 12:31:04 AM.
This article is licensed under a Creative Commons Attribution 3.0 Unported Licence.

theoretically expected value.[28–30,37] This implies that the redox mechanism of PNFE is not sufficiently described by the simple two-electron transfer shown in Fig. 4.

Electrochemical impedance spectra were recorded at different potentials within the potential range in which the redox activity was observed in the CVs to obtain further insights into the mechanism. The fitting of these spectra requires a physically meaningful EEC model. Fig. 5(A) shows the equivalent circuit describing the two-stage mechanism which is depicted in Fig. 4. This circuit model can be derived from the so-called Randles circuit modeling faradaic processes controlled by diffusion and kinetics.[39] The Randles circuit consists of the electrolyte uncompensated resistance R_U, the double layer capacity C_{dl}, the charge transfer resistance R_{ct}, and a semi-infinite Warburg element W accounting for diffusion. In this case, the diffusion limitations are assumed to arise due to local sodium-ion deficiencies within the pores of the slurry, as shown in Fig. 6. Though the concentration of sodium ions in the bulk electrolyte is very high, the movement through the smaller pores is likely diffusion-limited. In addition, the delocalization of the charge over the conjugated structure of the imide molecule affects mass transport as well. To account for the two stages of the mechanism, an adsorption capacitance $C_{a,2}$ and resistance $R_{a,2}$ are added to the Randles circuit.[34] Hereby, the model reflects the fact that the reduction of the first carbonyl group determines the second step of the redox process, which unquestionably takes place after the transfer of the first electron. Thus, the two stages are conjugated, and $C_{a,2}$, and $R_{a,2}$ are connected in the circuit accordingly. The impedance linked to the contribution of the film on the graphite substrate to the overall impedance response is accounted for by C_{geo} and R_{geo}.

In other words, this model describes a conjugated two-electron transfer with reversible stages, which corresponds to the mechanism shown in Fig. 4. It should be noted that the capacitative contribution could also be modeled with constant phase elements (CPEs) instead of capacitors. However, the direct physical meaning of the model is not clear, especially when multiple CPEs are used. In the case of the PNFE electrode, the fit quality does not improve significantly when C_{dl} or C_{geo} are replaced by CPEs. Furthermore, upon fitting, the exponent of the CPEs is very close to 1.00, indicating nearly ideal capacitative behavior. The resulting EEC depicted in Fig. 5(A) can be used to fit the data with high accuracy at potentials more positively than −300 mV.

Fig. 7 shows the impedance spectra at different potentials ranging from −300 mV *vs.* SSC to −1000 mV *vs.* SSC in Nyquist plots as well as the dependence of the phase shift Θ on the frequency. At −300 mV *vs.* SSC, the processes are fairly modeled by the two-stage mechanism. However, the spectra recorded at more negative electrode potentials within the region where faradaic processes take place do not support this model. At −400 mV and below, an additional contribution can be observed, leading to a different curvature in the transition region between high and low frequencies. This effect is even more distinctive in the Θ *vs.* frequency representation, which displays a different shape at these potentials. The exact origin of this is outside the scope of this manuscript as it does not influence the fitting statistics significantly.

Simultaneously to the primary two-stage conjugated mechanism, a one-electron single-stage mechanism was found to take place. This process can be modeled by a charge transfer resistance $R_{ct,1}$ and an adsorption capacitance $C_{a,1}$[34] that are connected in parallel to the elements representing the two-stage mechanism. By including these parameters, the spectra can be fitted with extremely high accuracy for all potentials, as shown in Fig. 7. This pathway is most likely linked to the formation of the stable radical anion after reduction by a single electron. This observation indicates that a certain portion of the polymer is not further reduced after this step. Reasons for this may be polymer–polymer or polymer–substrate interactions. Due to this effect, the experimental specific capacity of PNFE is expected to be lower than the theoretical specific capacity for a two-electron charge transfer as parts of the polymer only accept one electron. Therefore, the observed capacity losses serve as an important verification of the suggested EEC.

The fitting parameters and their respective errors for all potentials are given in Table S1 (ESI†). It shows that the charge transfer resistance of the two-stage conjugated pathway is significantly lower than the charge transfer resistance of the single-stage pathway. At all potentials, $R_{ct,1}$ is 5–10 times higher than $R_{ct,2}$, with the difference getting smaller towards lower potentials. Therefore, the two-electron mechanism is determined to be dominating, whereas the single-electron mechanism is mostly suppressed. At −300 mV *vs.* SSC, the difference is the largest, which is why the spectrum can also be fitted with the simpler circuit that is depicted in Fig. 5(A). However, at lower potentials, the ratio decreases, and the contribution of the single-stage mechanism becomes significant.

4. Conclusions

In conclusion, this research contributes to elucidating the charge storage mechanism of polyimides through the integration of CV and EIS analyses. The established two-step conjugated enolization mechanism has been definitively identified as the primary process governing this electrode material. Nevertheless, this investigation has unveiled a previously unrecognized single-electron pathway manifesting at potentials below −300 mV *vs.* SSC, challenging the completeness of the conventional model. This newly identified pathway, likely associated with the stabilization of radical anions post-initial reduction, provides crucial insights into the observed disparities between experimental and theoretical specific capacities.

The introduction of the electrochemical equivalent circuit (EEC) proposed in this study enables highly accurate and minimally error-prone fitting of impedance spectra for polyimide electrodes. Moreover, the implications extend beyond this specific material, as analogous organic electrode materials relying on enolization reactions can likely be similarly modeled. Consequently, the outcomes of this research offer a potent

© 2024 The Author(s). Published by the Royal Society of Chemistry

Open Access Article. Published on 21 March 2024. Downloaded on 5/25/2025 12:31:04 AM. This article is licensed under a Creative Commons Attribution 3.0 Unported Licence.

analytical tool for comprehending the processes within carbonyl-based electrode materials and batteries employing such electrodes.

Beyond its fundamental contributions, this work paves the way for more comprehensive EIS analyses, opening up novel avenues for monitoring degradation effects, cell aging, and various processes in a non-destructive manner. The knowledge gleaned from this study promises to be instrumental in advancing the understanding of organic electrode materials, ultimately contributing to the optimization and longevity of electrochemical systems.

Author contributions

R. S.: conceptualization, data curation, formal analysis, validation, investigation, visualization, methodology, writing – original draft, writing – review and editing. S. V.: investigation, writing – original draft, writing – review and editing. Y. G.: investigation, validation. B. R.: resources, supervision, funding acquisition. A. S. B.: conceptualization, resources, software, formal analysis, supervision, funding acquisition, writing – review and editing.

Conflicts of interest

There are no conflicts to declare.

Acknowledgements

The Authors acknowledge financial support from the Deutsche Forschungsgemeinschaft (DFG) in the framework of Germany's Excellence Strategy – EXC 2089/1-390776260, the cluster of excellence ''e-conversion''.

References

1 J. B. Goodenough, Electrochemical energy storage in a sustainable modern society, *Energy Environ. Sci.*, 2014, **7**, 14–18.
2 A. Kalair, N. Abas, M. S. Saleem, A. R. Kalair and N. Khan, Role of energy storage systems in energy transition from fossil fuels to renewables, *Energy Storage*, 2021, **3**, e135.
3 G. E. Blomgren, The Development and Future of Lithium Ion Batteries, *J. Electrochem. Soc.*, 2017, **164**, A5019–A5025.
4 M. Li, J. Lu, Z. Chen and K. Amine, 30 Years of Lithium-Ion Batteries, *Adv. Mater.*, 2018, e1800561.
5 D. Larcher and J.-M. Tarascon, Towards greener and more sustainable batteries for electrical energy storage, *Nat. Chem.*, 2015, **7**, 19–29.
6 E. A. Olivetti, G. Ceder, G. G. Gaustad and X. Fu, Lithium-Ion Battery Supply Chain Considerations: Analysis of Potential Bottlenecks in Critical Metals, *Joule*, 2017, **1**, 229–243.
7 Y. Wang, R. Chen, T. Chen, H. Lv, G. Zhu, L. Ma, C. Wang, Z. Jin and J. Liu, Emerging non-lithium ion batteries, *Energy Storage Mater.*, 2016, **4**, 103–129.
8 S.-W. Kim, D.-H. Seo, X. Ma, G. Ceder and K. Kang, Electrode Materials for Rechargeable Sodium-Ion Batteries: Potential Alternatives to Current Lithium-Ion Batteries, *Adv. Energy Mater.*, 2012, **2**, 710–721.
9 B. Qin, M. Wang, S. Wu, Y. Li, C. Liu, Y. Zhang and H. Fan, Carbon dots confined nanosheets assembled $NiCo_2S_4$@CDs cross-stacked architecture for enhanced sodium ion storage, *Chin. Chem. Lett.*, 2023, 108921.
10 Z.-Y. Gu, Y.-L. Heng, J.-Z. Guo, J.-M. Cao, X.-T. Wang, X.-X. Zhao, Z.-H. Sun, S.-H. Zheng, H.-J. Liang, B. Li and X.-L. Wu, Nano self-assembly of fluorophosphate cathode induced by surface energy evolution towards high-rate and stable sodium-ion batteries, *Nano Res.*, 2023, **16**, 439–448.
11 J.-Z. Guo, Z.-Y. Gu, M. Du, X.-X. Zhao, X.-T. Wang and X.-L. Wu, Emerging characterization techniques for delving polyanion-type cathode materials of sodium-ion batteries, *Mater. Today*, 2023, **66**, 221–244.
12 D. Xie, Y. Sang, D.-H. Wang, W.-Y. Diao, F.-Y. Tao, C. Liu, J.-W. Wang, H.-Z. Sun, J.-P. Zhang and X.-L. Wu, ZnF2 -Riched Inorganic/Organic Hybrid SEI: in situ-Chemical Construction and Performance-Improving Mechanism for Aqueous Zinc-ion Batteries, *Angew. Chem., Int. Ed.*, 2023, **62**, e202216934.
13 J.-L. Yang, J.-M. Cao, X.-X. Zhao, K.-Y. Zhang, S.-H. Zheng, Z.-Y. Gu and X.-L. Wu, Advanced aqueous proton batteries: working mechanism, key materials, challenges and prospects, *Energy Chem.*, 2022, **4**, 100092.
14 J.-Y. Hwang, S.-T. Myung and Y.-K. Sun, Sodium-ion batteries: present and future, *Chem. Soc. Rev.*, 2017, **46**, 3529–3614.
15 Nagmani, D. Pahari, P. Verma and S. Puravankara, Are Na-ion batteries nearing the energy storage tipping point? – Current status of non-aqueous, aqueous, and solid-sate Na-ion battery technologies for sustainable energy storage, *J. Energy Storage*, 2022, **56**, 105961.
16 F. Zhang, W. Zhang, D. Wexler and Z. Guo, Recent Progress and Future Advances on Aqueous Monovalent-Ion Batteries towards Safe and High-Power Energy Storage, *Adv. Mater.*, 2022, **34**, e2107965.
17 D. Kundu, E. Talaie, V. Duffort and L. F. Nazar, The emerging chemistry of sodium ion batteries for electrochemical energy storage, *Angew. Chem., Int. Ed.*, 2015, **54**, 3431–3448.
18 D. Bin, F. Wang, A. G. Tamirat, L. Suo, Y. Wang, C. Wang and Y. Xia, Progress in Aqueous Rechargeable Sodium-Ion Batteries, *Adv. Energy Mater.*, 2018, **8**, 1703008.
19 C. D. Wessells, R. A. Huggins and Y. Cui, Copper hexacyanoferrate battery electrodes with long cycle life and high power, *Nat. Commun.*, 2011, **2**, 550.
20 X. Lamprecht, P. Zellner, G. Yesilbas, L. Hromadko, P. Moser, P. Marzak, S. Hou, R. Haid, F. Steinberger, T. Steeger, J. M. Macak and A. S. Bandarenka, Fast-Charging Capability of Thin-Film Prussian Blue Analogue Electrodes for Aqueous Sodium-Ion Batteries, *ACS Appl. Mater. Interfaces*, 2023, **15**, 23951–23962.

© 2024 The Author(s). Published by the Royal Society of Chemistry

Open Access Article. Published on 21 March 2024. Downloaded on 5/25/2025 12:31:04 AM.
This article is licensed under a Creative Commons Attribution 3.0 Unported Licence.

21 F. Yin, Z. Liu, S. Yang, Z. Shan, Y. Zhao, Y. Feng, C. Zhang and Z. Bakenov, $Na_4Mn_9O_{18}$/Carbon Nanotube Composite as a High Electrochemical Performance Material for Aqueous Sodium-Ion Batteries, *Nanoscale Res. Lett.*, 2017, **12**, 569.
22 Y. Lu, X. Wu, Z. Li, H. Jiang, L. Liu, Q. Ban and L. Gai, Na^+/K^+-codoped amorphous manganese oxide with enhanced performance for aqueous sodium-ion battery, *J. Alloys Compd.*, 2023, **937**, 168344.
23 C. Ding, Z. Chen, C. Cao, Y. Liu and Y. Gao, Advances in Mn-Based Electrode Materials for Aqueous Sodium-Ion Batteries, *Nano-Micro Lett.*, 2023, **15**, 192.
24 T. Xu, M. Zhao, Z. Li, Z. Su, W. Ren, S. Yang and V. G. Pol, A High Rate and Long Cycling Performance NaTi 2 (PO 4) 3 Core–Shell Porous Nanosphere Anode for Aqueous Sodium-Ion Batteries, *Energy Technol.*, 2022, **10**, 2200970.
25 M. Wu, W. Ni, J. Hu and J. Ma, NASICON-Structured $NaTi_2(PO_4)_3$ for Sustainable Energy Storage, *Nano-Micro Lett.*, 2019, **11**, 44.
26 J. J. Shea and C. Luo, Organic Electrode Materials for Metal Ion Batteries, *ACS Appl. Mater. Interfaces*, 2020, **12**, 5361–5380.
27 C. Han, J. Zhu, C. Zhi and H. Li, The rise of aqueous rechargeable batteries with organic electrode materials, *J. Mater. Chem. A*, 2020, **8**, 15479–15512.
28 W. Deng, Y. Shen, J. Qian and H. Yang, A polyimide anode with high capacity and superior cyclability for aqueous Na-ion batteries, *Chem. Commun.*, 2015, **51**, 5097–5099.
29 T. Gu, M. Zhou, M. Liu, K. Wang, S. Cheng and K. Jiang, A polyimide–MWCNTs composite as high performance anode for aqueous Na-ion batteries, *RSC Adv.*, 2016, **6**, 53319–53323.
30 L. Chen, J. L. Bao, X. Dong, D. G. Truhlar, Y. Wang, C. Wang and Y. Xia, Aqueous Mg-Ion Battery Based on Polyimide Anode and Prussian Blue Cathode, *ACS Energy Lett.*, 2017, **2**, 1115–1121.
31 P. Iurilli, C. Brivio and V. Wood, On the use of electrochemical impedance spectroscopy to characterize and model the aging phenomena of lithium-ion batteries: a critical review, *J. Power Sources*, 2021, **505**, 229860.
32 M. Gaberšček, Understanding Li-based battery materials via electrochemical impedance spectroscopy, *Nat. Commun.*, 2021, **12**, 6513.
33 L. Jiang, Y. Lu, C. Zhao, L. Liu, J. Zhang, Q. Zhang, X. Shen, J. Zhao, X. Yu, H. Li, X. Huang, L. Chen and Y.-S. Hu, Building aqueous K-ion batteries for energy storage, *Nat. Energy*, 2019, **4**, 495–503.
34 X. Lamprecht, I. Evazzade, I. Ungerer, L. Hromadko, J. M. Macak, A. S. Bandarenka and V. Alexandrov, Mechanisms of Degradation of $Na_2Ni[Fe(CN)_6]$ Functional Electrodes in Aqueous Media: A Combined Theoretical and Experimental Study, *J. Phys. Chem. C*, 2023, **127**, 2204–2214.
35 A. S. Bandarenka, Development of hybrid algorithms for EIS data fitting, in *Lecture Notes on Impedance Spectroscopy. Measurement, Modeling and Applications*, ed. O. Kanoun, CRC Press, Tailor and Francis Group, London, 2013, vol. 4, pp. 29–36.
36 H. Banda, D. Damien, K. Nagarajan, M. Hariharan and M. M. Shaijumon, A polyimide based all-organic sodium ion battery, *J. Mater. Chem. A*, 2015, **3**, 10453–10458.
37 Y. Hu, H. Ding, Y. Bai, Z. Liu, S. Chen, Y. Wu, X. Yu, L. Fan and B. Lu, Rational Design of a Polyimide Cathode for a Stable and High-Rate Potassium-Ion Battery, *ACS Appl. Mater. Interfaces*, 2019, **11**, 42078–42085.
38 G. Hernández, N. Casado, R. Coste, D. Shanmukaraj, L. Rubatat, M. Armand and D. Mecerreyes, Redox-active polyimide–polyether block copolymers as electrode materials for lithium batteries, *RSC Adv.*, 2015, **5**, 17096–17103.
39 A. Lasia, *Electrochemical Impedance Spectroscopy and its Applications*, Springer New York, New York, NY, 2014.

© 2024 The Author(s). Published by the Royal Society of Chemistry